

Landmark and Intensity-Based, Consistent Thin-Plate Spline Image Registration

Hans J. Johnson and Gary E. Christensen

Department of Electrical and Computer Engineering,
The University of Iowa, Iowa City IA 52242, USA
hans-johnson@uiowa.edu, gary-christensen@uiowa.edu

Abstract. Landmark-based thin-plate spline image registration is one of the most commonly used methods for non-rigid medical image registration and anatomical shape analysis. It is well known that this method does not produce a unique correspondence between two images away from the landmark locations because interchanging the role of source and target landmarks does not produce forward and reverse transformations that are inverses of each other. In this paper, we present two new image registration algorithms that minimize the thin-plate spline bending energy and the inverse consistency error—the error between the forward and the inverse of the reverse transformation. The landmark-based consistent thin-plate spline algorithm registers images given a set of corresponding landmarks while the intensity-based consistent thin-plate spline algorithm uses both corresponding landmarks and image intensities. Results are presented that demonstrate that using landmark and intensity information to jointly estimate the forward and reverse transformations provides better correspondence than using landmarks or intensity alone.

1 Introduction

There are many image registration algorithms based on matching corresponding landmarks in two images [7]. The thin-plate spline image (TPS) registration technique pioneered by Fred Bookstein [1,4,2] is the most commonly used landmark driven image registration algorithm. Generalizations of this procedure include Kriging methods [11,10] that use regularization models other than the thin-plate spline (TPS) model, anisotropic landmark interactions [12], and directed landmarks [3].

The TPS algorithm (see Section 2.2) defines a unique smooth registration from a template image to a target image based on registering corresponding landmarks. Correspondence away from the landmark points is defined by interpolating the transformation with a TPS model. Although TPS interpolation produces a smooth transformation from one image to another, it does not define a unique correspondence between the two images except at the landmark points. This can be seen by comparing the transformation generated by matching a set of source landmarks to a set of target landmarks with the transformation

generated by matching the target landmarks to the template landmarks. If the correspondence is unique then the forward and reverse transformations will be inverses of one another (see Fig. 1). This is not the case as shown by the examples in Section 3. In this paper, the idea of consistent image registration [5,9,6] was

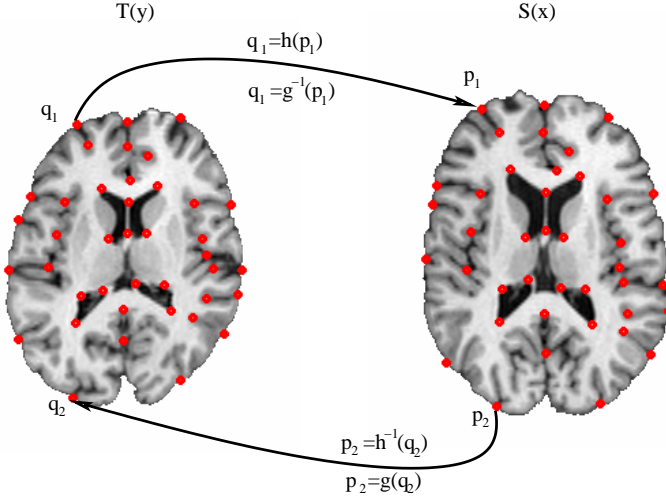


Fig. 1. Consistent image registration is based on the principle that the mappings h from T to S and g from S to T define a consistent point-by-point correspondence between the coordinate systems of T and S . Consistency is enforced mathematically by jointly estimating h and g while constraining h and g to be inverse mappings of one another.

combined with the thin-plate spline algorithm to overcome the problem that the forward and reverse transformations generated by the TPS algorithm are not inverses of one another. In the consistent image registration approach, the forward and reverse transformations between two images are jointly estimated subject to the constraints that they minimize the TPS bending energy and that they are inverses of one another. The merger of these two approaches produced a landmark-based consistent TPS (CL-TPS) and a landmark and intensity-based consistent TPS (CLI-TPS) image registration algorithms. The CL-TPS algorithm (see Section 2.3) provides a means to estimate a consistent pair of forward and reverse transformations given a set of corresponding points. The CLI-TPS algorithm (see Section 2.4) combines both landmark and intensity information to estimate a consistent pair of forward and reverse transformations.

2 Methods

2.1 Notation

Figure 1 shows two MRI images with corresponding landmarks that define the notation used throughout the paper. Assume that the template $T(y)$ and target $S(x)$ images are defined on the continuous domain $\Omega = [0, 1]^2$ and were constructed from $N_1 \times N_2$ pixel images using bilinear interpolation. Let $q_i \in \Omega$, and $p_i \in \Omega$, for $i = 1, \dots, M$, define corresponding landmarks in the template T and target S images, respectively. The forward transformation $h : \Omega \rightarrow \Omega$ is defined as the mapping that transforms T into the shape of S and the reverse transformation $g : \Omega \rightarrow \Omega$ is defined as the mapping that transforms S into the shape of T . The forward transformation $h(x) = x + u(x)$ defines the mapping from the coordinate system of the template to the target and the reverse transformation $g(y) = y + w(y)$ defines the mapping from the coordinate system of the target image to the template for $x, y \in \Omega^1$. The inverse of the forward transformation is defined as $h^{-1}(y) = y + \tilde{u}(y)$ and the reverse transformation is defined as $g^{-1}(x) = x + \tilde{w}(x)$.

2.2 Landmark-Based, Thin-Plate Spline Image Registration with Cyclic Boundary Conditions

The landmark-based, TPS image registration algorithm [1,4,2] registers a template image with a target image by matching corresponding landmarks identified in both images. Registration at non-landmark points is accomplished by interpolation such that the overall transformation smoothly maps the template into the shape of the target image.

In general, the landmark image registration problem can be thought of as a Dirichlet problem [10] and can be stated mathematically as finding the displacement field u that minimizes the cost function

$$C = \int_{\Omega} \|\mathcal{L}u(x)\|^2 dx \tag{1}$$

subject to the constraints that $u(p_i) = q_i - p_i$ for $i = 1, \dots, M$. The operator \mathcal{L} denotes a symmetric linear differential operator [8] and is used to interpolate u away from the corresponding landmarks. When $\mathcal{L} = \nabla^2$, the problem reduces to the TPS image registration problem given by

$$C = \int_{\Omega} \|\nabla^2 u(x)\|^2 dx = \sum_{i=1}^2 \int_{\Omega} \left(\frac{\partial^2 u_i(x)}{\partial x_1^2} \right)^2 + 2 \left(\frac{\partial^2 u_i(x)}{\partial x_1 \partial x_2} \right) + \left(\frac{\partial^2 u_i(x)}{\partial x_2^2} \right)^2 dx_1 dx_2 \tag{2}$$

subject to the constraints that $u(p_i) = q_i - p_i$ for $i = 1, \dots, M$.

¹ The mappings h and g are Eulerian coordinate system transformations

It is well known [1,4,2] that the TPS displacement field $u(x)$ that minimizes the bending energy defined by Eq. 2 has the form

$$u(x) = \sum_{i=1}^M \xi_i \phi(x - p_i) + Ax + b. \tag{3}$$

where $\phi(r) = r^2 \log r$ and ξ_i are 2×1 weighting vectors. The 2×2 matrix $A = [a_1, a_2]$ and the 2×1 vector b define the affine transformation where a_1 and a_2 are 2×1 vectors.

The unknown parameters $W = [\xi_1, \dots, \xi_M, a_1, a_2, b]^T$ are determined by substituting the landmark constrains into Eq. 3 and solving the resulting equations. Let $\phi_{i,j} = \phi(|p_i - q_j|)$ build the matrix

$$K = \begin{bmatrix} \Phi & A \\ A^T & O \end{bmatrix} \quad \text{where} \quad \Phi = \begin{bmatrix} \phi_{1,1} & \phi_{1,2} & \dots & \phi_{1,M} \\ \phi_{2,1} & \phi_{2,2} & \dots & \phi_{2,M} \\ \vdots & \vdots & \ddots & \vdots \\ \phi_{M,1} & \phi_{M,2} & \dots & \phi_{M,M} \end{bmatrix}, \quad A = \begin{bmatrix} p_{1,1} & p_{1,2} & 1 \\ p_{2,1} & p_{2,2} & 1 \\ \vdots & \vdots & \vdots \\ p_{M,1} & p_{M,2} & 1 \end{bmatrix}, \tag{4}$$

and O is a 3×3 matrix of zeros. Also, define the $(M + 3) \times 2$ matrix of landmark displacements as $D = [d_1, \dots, d_M, 0, 0, 0]^T$ where $d_i = q_i - p_i$ for $i = 1, \dots, M$. The equations formed by substituting the landmark constrains into Eq. 3 can be written in matrix form as $D = KW$. The solution W to this matrix equation is determined by least squares estimation since the matrix K is not guaranteed to be full rank.

The TPS interpolant $\phi(r) = r^2 \log r$ is derived assuming infinite boundary conditions, i.e., Ω is assumed to be the whole plane R^2 in Eq. 2. A TPS transformation is truncated at the image boundary when it is applied to an image. This presents a mismatch in boundary conditions at the image edges when comparing forward and reverse transformations between two images. It also implies that a TPS transformation is not an one-to-one and onto mapping between two image spaces. To overcome this problem and to match the cyclic boundary conditions assumed by the intensity-based consistent image registration algorithm [5,6], we use the following procedure to approximate cyclic boundary conditions for the TPS algorithm.

Figure 2 illustrates the concept of cyclic boundary conditions for the landmark TPS registration problem. Cyclic boundary conditions implies a toroidal coordinate system such that the left-right and top-bottom boundaries of the domain Ω are mapped together. Modifying the boundary conditions in this manner causes an infinite number of interactions between landmarks for a given finite set of landmark points. Panel (b) shows two such interactions between landmark points p_1 and p_2 ; one within the domain Ω and another between adjacent domains. It is not practical to solve Eq. 4 with the resulting infinite dimensional matrix, so the cyclic boundary conditions are approximated by replicating the landmark locations in the eight adjacent domains as shown in panel (b) of Fig. 2.

This provides a good approximation to cyclic boundary conditions since the kernel function, $\phi(r) = r^2 \log r$, causes interactions between landmarks to decrease rapidly as the distance between landmarks increases. In our tests, there

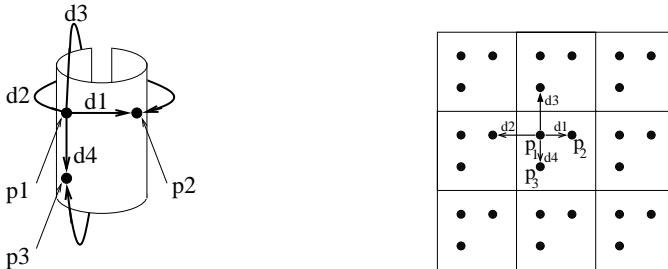


Fig. 2. Diagrams describing the coordinate system and points used to ensure that the resulting displacement field demonstrates continuous cyclic boundary conditions. The left panel is a depiction of the toroidal coordinate system. The right panel shows the layout of the point used to solve the TPS with approximate circular boundaries.

were significant differences between the transformations found using infinite and cyclic boundary conditions but there was nearly no difference in terms of the magnitude of the fiducial landmark errors. The major differences between the two sets of boundary conditions was in the location of the maximum inverse consistency error. The maximum inverse consistency error was located on the image boundaries in the case of infinite boundary conditions while it was away from the boundaries for the case of cyclic boundary conditions (see Fig. 4).

2.3 Landmark Consistent Thin-Plate Spline Registration

The CL-TPS image registration is solved by minimizing the cost function given by

$$\begin{aligned}
 C = & \rho \int_{\Omega} \|\mathcal{L}u(x)\|^2 + \|\mathcal{L}w(x)\|^2 dx + \chi \int_{\Omega} \|u(x) - \tilde{w}(x)\|^2 + \|w(x) - \tilde{u}(x)\|^2 dx \\
 & + \sum_{i=1}^M \zeta_i \|p_i + u(p_i) - q_i\|^2 + \zeta_i \|q_i + w(q_i) - p_i\|^2.
 \end{aligned}
 \tag{5}$$

The first integral of the cost function defines the bending energy of the TPS for the displacement fields u and w associated with the forward and reverse transformations, respectively. The second integral is called the inverse consistency constraint (ICC) and is used to enforce that the forward and reverse transformations are inverses of one another. The third term of the cost function defines the correspondence between the normalized landmarks and is minimized when

$p_i + u(p_i) = q_i$ and $q_i + w(q_i) = p_i$ for $i = 1, \dots, M$. The constants ρ , χ , and ζ_i define the relative importance of each term of the cost function.

Equation 5 must be minimized numerically since the inverse consistency constraint is a function of the inverse-forward $h^{-1}(x) = x + \tilde{u}(x)$ and inverse-reverse $g^{-1}(x) = x + \tilde{w}(x)$ transformations. To do this, Eq. 5 is discretized. Define the landmark locations $\bar{p}_i = [N_1 p_{i,1}, N_2 p_{i,2}]^T$ and $\bar{q}_i = [N_1 q_{i,1}, N_2 q_{i,2}]^T$ to be the landmark coordinates in the space of the original $N_1 \times N_2$ pixel images. Let $\Omega_d = \{(n_1, n_2) | 0 \leq n_1 < N_1; 0 \leq n_2 < N_2; \text{ and } n_1, n_2 \text{ are integers}\}$ represent a discrete lattice of indexes associated with the pixel coordinates of the discrete images T and S . Let $\Omega'_d = \Omega_d \setminus \{\bar{p}_1, \dots, \bar{p}_M\}$ and $\Omega''_d = \Omega_d \setminus \{\bar{q}_1, \dots, \bar{q}_M\}$ represent the points in Ω_d not including the target and template landmark points, respectively. The discrete version of Eq. 5 is given by

$$\begin{aligned}
 C = & \frac{\rho}{N_1 N_2} \sum_{n \in \Omega'_d} \|\mathcal{L}u_d[n]\|^2 + \frac{\rho}{N_1 N_2} \sum_{n \in \Omega''_d} \|\mathcal{L}w_d[n]\|^2 \\
 & + \frac{\chi}{N_1 N_2} \sum_{n \in \Omega_d} \|u_d[n] - \tilde{w}_d[n]\|^2 + \|w_d[n] - \tilde{u}_d[n]\|^2 \\
 & + \sum_{i=1}^M \zeta_i \|p_i + u_d[\bar{p}_i] - q_i\|^2 + \zeta_i \|q_i + w_d[\bar{q}_i] - p_i\|^2 \tag{6}
 \end{aligned}$$

where $h_d[n] = h(\frac{n}{N}) = \frac{n}{N} + u(\frac{n}{N}) = \frac{n}{N} + u_d[n]$ is the discrete forward transformation and $g_d[n] = g(\frac{n}{N}) = \frac{n}{N} + w(\frac{n}{N}) = \frac{n}{N} + w_d[n]$ is the discrete reverse transformation. The notation $\frac{n}{N}$ is defined as the 2×1 column vector $[\frac{n_1}{N_1}, \frac{n_2}{N_2}]^T$ for $n \in \Omega_d$.

The last term of Eq. 6 places constraints on the displacement fields u and w at the landmark locations. This term effectively produces a soft constraint at the landmarks so that there does not have to be exact correspondence. The first two summations of Eq. 6 places constraints on the displacement fields u and w at each point of the discretized domain Ω_d except at the landmark locations. These terms penalize large derivatives of the displacement fields at all of the non-landmark points which effectively interpolates a smooth displacement field between the landmark points.

The discrete displacement fields are defined to have the form

$$u_d[n] = \sum_{k \in \Omega_d} \mu[k] e^{j \langle n, \theta[k] \rangle} \quad \text{and} \quad w_d[n] = \sum_{k \in \Omega_d} \eta[k] e^{j \langle n, \theta[k] \rangle} \tag{7}$$

for $n \in \Omega_d$ where the basis coefficients $\mu[k]$ and $\eta[k]$ are (2×1) complex-valued vectors and $\theta[k] = [\frac{2\pi k_1}{N_1}, \frac{2\pi k_2}{N_2}]^T$. The basis coefficients have the property that they have complex conjugate symmetry, i.e., $\mu[k] = \mu^*[N - k]$ and $\eta[k] = \eta^*[N - k]$. The notation $\langle \cdot, \cdot \rangle$ denotes the dot product of two vectors such that $\langle n, \theta[k] \rangle = \frac{2\pi k_1 n_1}{N_1} + \frac{2\pi k_2 n_2}{N_2}$.

The forward and reverse Fourier series parameterized displacement fields are initialized with the TPS solution found by Eq. 3 using

$$\mu[k] = \sum_{n \in \Omega_d} u_d[n] e^{-j \langle n, \theta[k] \rangle} \quad \text{and} \quad \eta[k] = \sum_{n \in \Omega_d} w_d[n] e^{-j \langle n, \theta[k] \rangle} \quad (8)$$

where $u_d[n] = u(\frac{n}{N})$ and $w_d[n] = w(\frac{n}{N})$ are given by Eq. 3 for the forward and reverse transformations, respectively.

The minimizer of Eq. 5 is determined by gradient descent.

2.4 Intensity-Based Consistent Thin-Plate Spline Registration with Landmark Thin-Plate Spline Initialization

The landmark and intensity-based consistent registration algorithm generalizes the consistent image registration presented in [5,9,6] to include landmark constraints. It is based on minimizing the cost function given by

$$C = \sigma \int_{\Omega} |T(h(x)) - S(x)|^2 + |S(g(x)) - T(x)|^2 dx \quad (9)$$

$$+ \rho \int_{\Omega} \|\mathcal{L}u(x)\|^2 + \|\mathcal{L}w(x)\|^2 dx + \chi \int_{\Omega} \|u(x) - \tilde{w}(x)\|^2 + \|w(x) - \tilde{u}(x)\|^2 dx$$

subject to the constraints that $u(p_i) = q_i - p_i$ and $w(q_i) = p_i - q_i$ for $i = 1, \dots, M$. The intensities of T and S are assumed to be scaled between 0 and 1. The first integral of the cost function defines the cumulative squared error similarity cost between the transformed template $T(h(x))$ and target image $S(x)$ and between the transformed target $S(g(y))$ and the template image $T(y)$. To use this similarity function, the images T and S must correspond to the same imaging modality and they may require pre-processing to equalize the intensities of the image. This term defines the correspondence between the template and target images as the forward and reverse transformations h and g , respectively, that minimized the squared error intensity differences between the images. The second integral is used to regularize the forward and reverse displacement fields u and w , respectively. This term is minimized for TPS transformations. The third integral is called the inverse consistency constraint and is minimized when the forward and reverse transformations h and g , respectively, are inverses of each other. The last term is the landmark constraint that keeps the landmarks aligned. The constants $\sigma, \rho, \chi, \zeta_i$ define the relative importance of each term of the cost function.

As in the previous section, the cost function in Eq. 10 must be discretized in order to numerically minimize it. The forward and reverse transformations h and g and their associated displacement fields u and w are parameterized by the discrete Fourier series defined by Eq. 7. The basis coefficients $\mu[k]$ and $\eta[k]$ of the forward and reverse displacement fields are initialized with the result of the CL-TPS algorithm. The discretized version of Eq. 10 is then minimized using gradient descent as described in [5,6].

3 Results

3.1 Landmark Registration

The eight corresponding landmarks shown in Fig. 3 will be used to demonstrate the landmark-based consistent TPS (CL-TPS) algorithm. In this example, the four inner landmarks correspond to the four outer landmarks and the four corner landmarks in both images correspond to each other. The forward transformation h is defined as the transformation, in Eulerian coordinates, that maps the four inner points to the four outer points causing an expansion of the grid in the center of the image. The reverse transformation g maps the outer points to the inner points causing a contraction of the grid in the center of the image.

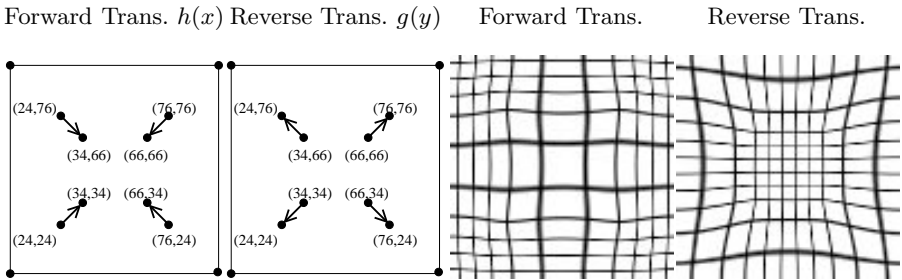


Fig. 3. The location of local displacements at the landmarks points for the forward, and reverse transformations of images with 100×100 pixels. Application of the TPS deformation fields to uniformly spaced grids for the forward and reverse transformations.

The top row of Fig. 4 shows the locations and magnitudes of the inverse errors after application of TPS interpolation to the landmarks in the forward and reverse directions. In these images, B and D point to landmark locations in the forward and reverse transformations respectively, B' and D' point to locations adjacent to landmarks, and A and C point to non-landmark locations. The inverse consistency errors associated with each of these points is listed in tables to the right of the images. The inverse consistency error at the landmark points is nominal both with and without enforcing the inverse consistency constraint (ICC). The bottom row of Fig. 4 shows that the ICC reduces the inverse consistency error uniformly across the displacement fields. The ICC has the least effect on inverse consistency errors at points in the neighborhood of landmarks.

A pair of transformations are point-wise consistent if the mapping of a point through the composite function $h(h^{-1}(x_i))$ maps x_i to itself. Any deviation from this identity mapping is a point-wise consistent error. By applying this composite mapping to a uniformly spaced grid one can visualize the magnitude, location, and direction of the point-wise inconsistencies as is shown in Fig. 5. The left

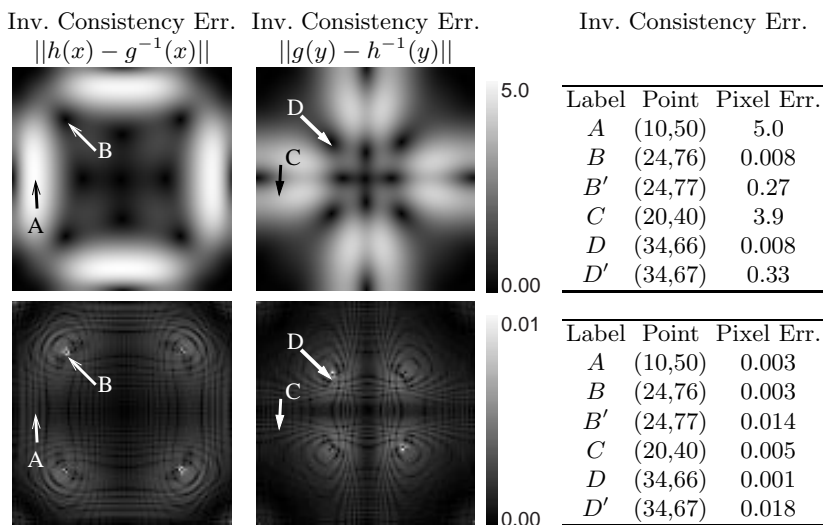


Fig. 4. The left and center panels are the inverse errors due to the forward and reverse transformation, respectively. The right panels are tables listing the fiducial errors associated with selected image points. The top row and bottom rows are the inverse consistency errors associated with TPS interpolation and CL-TPS, respectively.

panel shows that there is a considerable amount of inverse error in the TPS interpolant. The right panel shows that application of the inverse consistency constraint has reduced the point-wise consistency error considerably.

Table 1 reports that the CL-TPS algorithm reduced the maximum and average inverse consistency error by a factor of 277 and 740 times, respectively, as compared to the TPS algorithm. The trade-off for this gain was that the average fiducial error increases by a factor of 2, but this is still small relative to the pixel size. The Jacobian error calculated as $\frac{1}{2}|\min\{Jac(h)\} - 1/\max\{Jac(g)\}| + \frac{1}{2}|\min\{Jac(g)\} - 1/\max\{Jac(h)\}|$ provides an indirect measure of the inconsistency between the forward and reverse transformations. The Jacobian error is zero if the forward and reverse transformations are inverses of one another, but the converse is not true. Notice that the Jacobian error was five times smaller for the CL-TPS algorithm compared to the TPS algorithm.

3.2 Landmark and Intensity Registration

In this section we investigate the use of landmark registration on intensity-based images. Corresponding 64×80 isotropic 4 millimeter pixel 2D slices from a set of MRI acquired brains were used in this experiment. A set of 41 corresponding landmarks were manually defined as shown in Fig. 1.

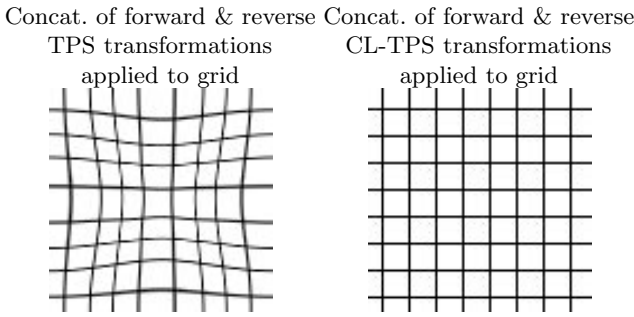


Fig. 5. Deformed grids showing the error between the forward and reverse transformations estimated with the landmark-based TPS algorithm(left panel) and the CL-TPS algorithm(right panel). The grids were deformed by the transformation constructed by composing the forward and reverse transformations together, i.e., $g(h(x))$. Ideally, the composition of the forward and reverse transformations is the identity mapping which produces no distortion of the grid as in the right panel.

In the first of four experiments the set of landmark points are used to perform the landmark TPS registration as in the in the previous section 3.1. The next experiment used the CL-TPS algorithm to register the two images. The third experiment is initialized with the results from the CL-TPS, but adds the image intensity as a driving force for the CLI-TPS registration. In each of the consistent registrations the ICC, landmark, TPS, and similarity constraints are imposed by iterative estimation of the Fourier series parameters for a total of 2000 iterations. In practice only the lowest $\frac{1}{8}$ harmonics, 8 and 10 harmonics in x and y directions respectively, of the Fourier series parameters are estimated.

The final experiment is an CI-TPS registration, and uses no landmark information in the estimation of the transformation parameters. It should be noted

Table 1. Comparison between Thin-plate spline image registration with and without the inverse consistency constraint (ICC). The table columns are the Experiment, (ICC), transformation Direction (TD), average fiducial error (AFE) in pixels, maximum inverse error (MIE) in pixels, average inverse error (AIE) in pixels, minimum jacobian value (MJ), inverse of the maximum jacobian value (IJ), and the jacobian error (JE).

Experiment	ICC	TD	AFE	MIE	AIE	MJ	IJ	JE
Landmark TPS	No	Forward	0.00004	5.0	2.2	0.25	0.43	0.13
		Reverse	0.00004	4.3	2.0	0.24	0.32	
CL-TPS	Yes	Forward	0.0008	0.012	0.0031	0.29	0.33	0.025
		Reverse	0.0008	0.011	0.0027	0.28	0.29	

that for this experiment, estimation of the Fourier parameters is limited to the first 2 harmonics initially, and is incremented to include additional harmonics after every 250 iterations. This has the effect of doing a global registration first and progressively becoming more local with each harmonic parameter added to the estimation. This approach allows for a much faster convergence of the parameters. It should also be observed that this approach stagnated in a local minima after 7 harmonics are estimated, and that the estimation of additional parameters had only marginal effects on the results.

The results were computed on a 667MHz, 21264 alpha processor. The landmark-based TPS registration took about 4 seconds to compute, the CL-TPS and CLI-TPS registrations took approximately 12 minutes to compute, and the CI-TPS registration took less than 3 minutes to compute. Figure 6 is a comparison

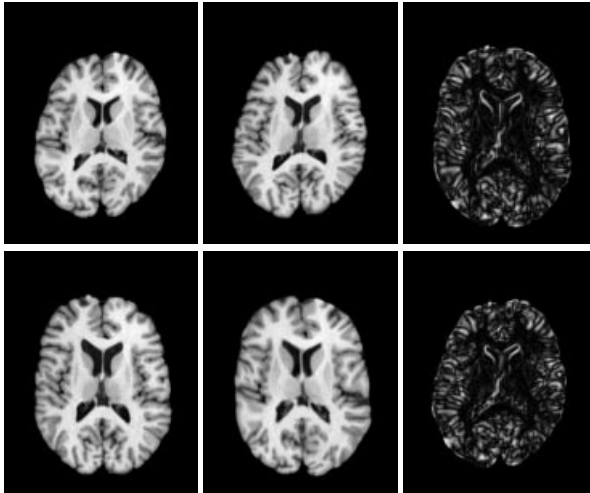


Fig. 6. Comparison of deformed images to originals when TPS initialization, inverse consistency, landmark, and similarity constraints are imposed. The left panels are the original images, the center panels are the deformed images, and the right panels are the absolute difference images between the original and deformed images.

of deformed images to originals from the CL-TPS and CLI-TPS registration. The left panels are the original images, the center panels are the deformed images, and the right panels are the absolute difference images between the original and deformed images. These images demonstrate that the deformed images closely match the appearance of the original images. From Table 2 it can be seen that the two consistent intensity-based registrations obtain almost identical average intensity both with and without the landmark constraints. The deformed and

absolute difference images for the consistent intensity-based registration are indistinguishable from those in Fig. 6.

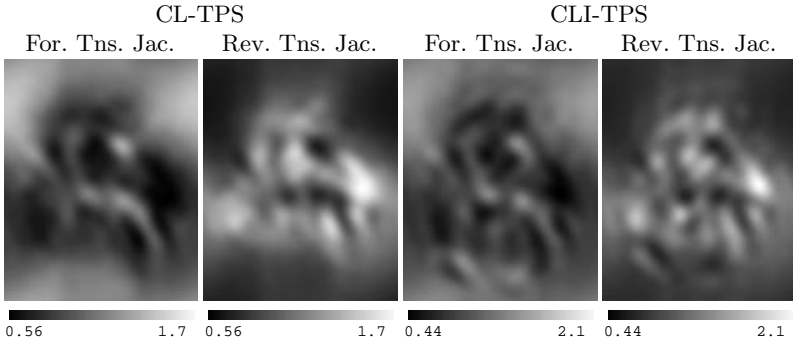


Fig. 7. Jacobian images that show locations of deformation for both CL-TPS(left two panels) and CLI-TPS(right two panels). Bright pixels represent expansion, and dark pixels represent contractions.

The image intensity difference between the original and deformed images for the intensity-based consistent TPS registrations with and without the landmark constraints are similar, but the transformations used in attaining the deformed images have different properties. Figure 7 are images displaying the Jacobian values at each pixel location for the landmark-based consistent TPS with and without the intensity constraints. The magnitude of local displacement is encoded such that bright pixels represent expansion, and dark pixels represent contractions. Notice that combining the intensity information with the landmark information provides additional local deformation as compared to just using the landmark information alone.

The inverse error images for the intensity-based consistent TPS registrations with and without the landmark constraints are shown in Fig. 8. Notice that the inverse consistency error is distributed uniformly across the image domain in both cases. However, the magnitude of the inverse consistency error is one third as large in the landmark constrained case.

Table 2 is a summary of representative statistics that can be taken from each of the experiments. From this table, the TPS and CL-TPS show that the addition of ICC can improve the inverse consistency of the transformations with only a small degradation of the fiducial landmark matching. It should be noted that the inverse consistency error in the TPS initialization tends to be larger as one moves away from landmarks and that inverse consistency error associated with the TPS interpolation can be decreased by defining more points of correspondence manually. The CLI-TPS uses intensity information to refine the transformation resulting from the CL-TPS. Table 2 demonstrates that the CLI-TPS registration has the smallest average intensity difference, but the largest

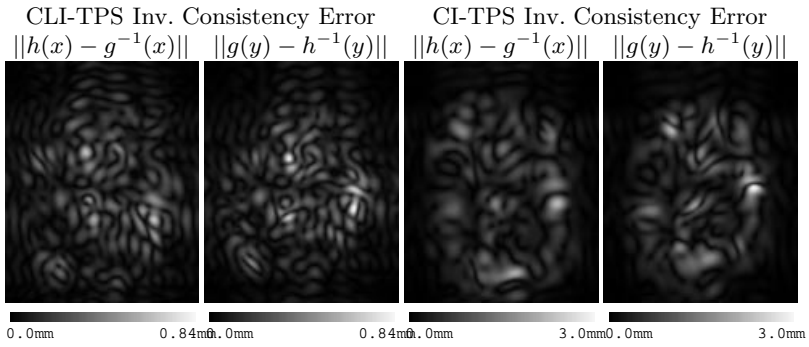


Fig. 8. Images that display the magnitude of inverse consistency errors for both CLI-TPS(left two panels) and CI-TPS(right two panels).

fiducial landmark errors. The CLI-TPS has marginally larger average intensity difference, but much smaller fiducial landmark errors. It should be noted that the large number of landmarks used in the CLI-TPS registration limits the effect of the intensity driving force in neighborhoods of the landmarks. In practice, when the the landmark points are more sparse the intensity driving force plays a more important role.

4 Summary and Conclusions

This work presented two new image registration algorithms based on thin-plate spline regularization: landmark-based, consistent thin-plate spline (TPS) image registration and landmark and intensity-based consistent TPS image registration. It was shown that the inverse consistency error between the forward and reverse transformations generated from the traditional TPS algorithm could be minimized using the landmark-based, consistent TPS algorithm. Inverse consistency error images showed that the largest error occurred away from the landmark points for the traditional TPS algorithm and near the landmark points for the consistent TPS algorithm. The average inverse consistency error was reduced by 100 times in the inner-to-outer dots example and greater than 15 times in the MRI brain example. The maximum inverse consistency error was reduced by almost 500 times for the inner-to-outer dots example but only 10 times for the MRI brain example. The Jacobian error was reduced from 0.13 to 0.025 for the inner-to-outer dots example and from 0.1 to 0.0 for the MRI brain example. The trade-off between better inverse consistency was that the fiducial error increased by over ten times in both examples. Using landmark and intensity information with the MRI brain example gave a better correspondence between the images than just using the landmark information as shown by a decrease in the average intensity difference. It was shown that using landmark and intensity information gave a better registration of the MRI brain images than just using the inten-

Table 2. Comparison between registering two 64×80 pixel MRI images with 41 landmarks, as shown in Fig. 1, using Landmark-based TPS, CL-TPS, CLI-TPS, and CI-TPS registration algorithms. The table columns are the 2D MRI Experiment, landmark initialization(LI), inverse consistence constraint (ICC), similarity constraint (SC). transformation Direction (TD), average fiducial error (AFE) in pixels, maximum inverse error (MIE) in pixels, average inverse error (AIE) in pixels, average intensity difference (AID), minimum jacobian value (MJ), inverse of the maximum jacobian value (IJ), and the jacobian error (JE).

2D MRI Exp.	LI	ICC	SC	TD	AFE	MIE	AID	AIE	MJ	IJ	JE
Landmark TPS	Yes	No	No	Forward	0.060	9.2	1.1	0.014	0.41	0.67	0.1
				Reverse	0.060	7.2	1.2	0.012	0.61	0.55	
CL-TPS	Yes	Yes	No	Forward	1.3	0.48	0.066	0.011	0.56	0.66	0.0
				Reverse	1.4	0.56	0.062	0.0096	0.66	0.56	
CLI-TPS	Yes	Yes	Yes	Forward	1.4	0.72	0.10	0.0081	0.44	0.66	0.25
				Reverse	1.5	0.84	0.10	0.0067	0.65	0.48	
CI-TPS	No	Yes	Yes	Forward	3.3	2.4	0.33	0.0049	0.34	0.56	0.125
				Reverse	3.6	3.0	0.31	0.0049	0.47	0.48	

sity information for the following measures: the average fiducial error, Jacobian error, maximum inverse error, and average inverse error.

Acknowledgments

We would like to thank John Haller and Michael W. Vannier of the Department of Radiology, The University of Iowa for providing the MRI data. This work was supported in part by the NIH grant NS35368 and a grant from the Whitaker Foundation.

References

1. F.L. Bookstein. *The Measurement of Biological Shape and Shape Change*, volume 24. Springer-Verlag: Lecture Notes in Biomathematics, New York, 1978.
2. F.L. Bookstein. Linear methods for nonlinear maps: Procrustes fits, thin-plate splines, and the biometric analysis of shape variability. In A. Toga, editor, *Brain Warping*, pages 157–181. Academic Press, San Diego, 1999.
3. F.L. Bookstein and W.D.K. Green. Edge information at landmarks in medical images. In Richard A. Robb, editor, *Visualization in Biomedical Computing 1992*, pages 242–258. SPIE 1808, 1992.
4. Fred L. Bookstein. *Morphometric Tools for Landmark Data*. Cambridge University Press, New York, 1991.
5. G.E. Christensen. Consistent linear-elastic transformations for image matching. In A. Kuba and M. Samal, editors, *Information Processing in Medical Imaging*, LCNS 1613, pages 224–237. Springer-Verlag, June 1999.

6. G.E. Christensen and H.J. Johnson. Consistent image registration. *Submitted to IEEE Transactions on Medical imaging*, 1999.
7. I.L. Dryden and K.V. Mardia. *Statistical Shape Analysis*. Wiley, New York, NY, 1 edition, September 1998.
8. U. Grenander and M. I. Miller. Computational anatomy: An emerging discipline. *Quarterly of Applied Mathematics*, LVI(4):617–694, December 1998.
9. Hans J. Johnson. Method for consistent linear-elastic medical image registration. Master's thesis, Department of Electrical and Computer Engineering, The University of Iowa, Iowa City, IA 52242, May 2000.
10. S.C. Joshi, M.I. Miller, G.E. Christensen, A. Banerjee, T.A. Coogan, and U. Grenander. Hierarchical brain mapping via a generalized Dirichlet solution for mapping brain manifolds. In R.A. Meltzer, A.Y. Wu, F.L. Bookstein, and W.D. Green, editors, *Vision Geometry IV*, Proceedings of SPIE Vol. 2573, pages 278–289, 1995.
11. J.T. Kent and K.V. Mardia. The link between kriging and thin-plate splines. In F.P. Kelly, editor, *Probability, Statistics and Optimisation*. John Wiley and Sons, 1994.
12. K. Rohr, M. Fornefett, and H.S. Stiehl. Approximating thin-plate splines for elastic registration: Integration of landmark errors and orientation attributes. In A. Kuba and M. Samal, editors, *Information Processing in Medical Imaging*, LCNS 1613, pages 252–265. Springer-Verlag, June 1999.